



# Inclusion of Isomers/Astromers in *s*-process Nucleosynthesis: The Pivotal Case of $^{85}\text{Kr}$

Jaad A. Tannous<sup>1</sup> , G. Wendell Misch<sup>2,3</sup> , Matthew R. Mumpower<sup>2,3</sup> , Bradley S. Meyer<sup>1</sup> , F. X. Timmes<sup>4</sup> ,  
Aaron Couture<sup>5</sup> , and Chris L. Fryer<sup>6</sup>

<sup>1</sup> Department of Physics and Astronomy, Clemson University, Clemson, SC 29634, USA; [jtannou@g.clemson.edu](mailto:jtannou@g.clemson.edu)

<sup>2</sup> Theoretical Division, Los Alamos National Laboratory, Los Alamos, NM 87545, USA

<sup>3</sup> Center for Theoretical Astrophysics, Los Alamos National Laboratory, Los Alamos, NM 87545, USA

<sup>4</sup> School of Earth and Space Exploration, Arizona State University, Tempe, AZ 85287, USA

<sup>5</sup> Physics Division, Los Alamos National Laboratory, Los Alamos, NM 87545, USA

<sup>6</sup> Center for Nonlinear Studies, Los Alamos National Laboratory, Los Alamos, NM 87545, USA

Received 2024 September 26; revised 2025 April 9; accepted 2025 April 20; published 2025 June 10

## Abstract

$^{85}\text{Kr}$  is an *s*-process branch point nucleus: the competition between neutron capture and  $\beta$  decay influences the production of nearby nuclides. Its evolution is complicated by the existence of a long-lived isomer that  $\beta$ -decays on a much shorter timescale than the ground state. We calculate the effective thermal transition rates between the ground and isomeric states along with estimates of their thermal  $\beta$ -decay rates in a suite of nucleosynthesis computations to assess the consequences of this isomer on isotopic abundances. A central finding in this study is that the *s*-process flow with the isomer included under astrophysical conditions relevant for the *s*-process creates a shift in abundance yield of the important radioactivity  $^{87}\text{Rb}$  by a factor of  $\sim 2.4$  relative to the case when the  $^{85}\text{Kr}$  is taken to be internally equilibrated when neutron exposures approach the main branch limit. On the other hand, the  $^{88}\text{Sr}/^{86}\text{Sr}$  ratio is little affected because the bulk of the flow through  $^{85}\text{Kr}$  is still via beta decay, whether the isomer is taken into account or not.

*Unified Astronomy Thesaurus concepts:* Nuclear astrophysics (1129); Stellar nucleosynthesis (1616); *S*-process (1419)

## 1. Introduction

The excited nuclear states of isotopes come into play in astrophysics due to the high temperature and density environments. Depending on the astrophysical setting, models have employed nuclear reaction networks that typically only considered either the ground state, such as in stellar evolution, or a Boltzmann distribution, as in supernova calculations. When a species has an isomeric state, however, it can fail to reach a Boltzmann distribution, raising the need for separate treatment (R. A. Ward & W. A. Fowler 1980). Examples of species known to exhibit such behavior include  $^{26}\text{Al}$ ,  $^{85}\text{Kr}$ , and  $^{180}\text{Ta}$ , each of which contains long-lived excited states with large spin differences from the ground state, inhibiting deexcitation. When isomers fail to equilibrate in astrophysical settings, they are called astromers (G. W. Misch et al. 2020). From an astronomical standpoint, astromers exhibit unique signatures spectroscopically, and their effects can be inferred in presolar grain abundances (T. Lee et al. 1977). Much headway has been made to develop frameworks for handling isomers from a nuclear structure standpoint, motivated by  $^{26}\text{Al}$  (T. H. Handley & W. S. Lyon 1955; S. S. Gupta & B. S. Meyer 2001; R. Diehl et al. 2006; S. Almaraz-Calderon et al. 2017). See G. W. Misch & M. R. Mumpower (2024) for a recent review.

Our interest here is in analyzing the effect of the  $^{85}\text{Kr}$  isomer on slow neutron-capture process (*s*-process). In the *s*-process,  $\beta$ -unstable isotopes typically capture neutrons more slowly than they beta decay. For some nuclides such as  $^{85}\text{Kr}$ , known as branching species, however, the neutron-capture timescale can

compete with that for beta decay, and the network flow “branches” at this species. Since isomers often have different half-lives than their respective ground states, inclusion of isomers in a nuclear reaction network can affect the relative neutron-capture and beta-decay flows through a branching species, which, in turn, affects relative downstream abundances or even leads to alternate routes taken to reach the *s*-process terminal loop near  $^{208}\text{Pb}$ . For our study, we focus on  $^{85}\text{Kr}$  for two reasons. First, it does not thermalize until temperature  $T \sim 20\text{--}25$  keV (G. W. Misch et al. 2021), a range well within *s*-process parameters. The mass density,  $\rho$ , where *s*-process occurs typically ranges between  $10^3$  and  $10^5$  g cm $^{-3}$ , all dependent on mass, stage, metallicity, and other physical properties; see D. Hollowell & I. Iben (1990) and U. Frischknecht et al. (2015). Second, it is a pivotal isotope that can lead to various shifts in abundance yields for rubidium and strontium isotopes.

Figure 1 shows the *s*-process network in the vicinity of  $^{85}\text{Kr}$ . The neutron-capture route to  $^{86}\text{Kr}$  occurs either through the ground or isomeric state. These states also beta decay to  $^{85}\text{Rb}$ , with the ground state living 10.739 yr and the isomer 4.48 hr. If the two states are not in thermal equilibrium in the isotope, branching is less likely if more material is in the isomer than the ground state owing to the former’s shorter beta-decay lifetime. The *s*-process branching at  $^{85}\text{Kr}$  to  $^{86}\text{Kr}$  leads to production of  $^{87}\text{Rb}$ , an important cosmochronometer with a lifetime of 49.7 Gyr (J. L. Birck & C. J. Allegre 1978). N. Prantzos et al. (2020) conclude that 96% of  $^{87}\text{Rb}$  was produced in the *s*-process, so a proper accounting for the *s*-process branching at  $^{85}\text{Kr}$  is essential for a full understanding of the Galactic chemical evolution of  $^{87}\text{Rb}$ .

The *s*-process branching at  $^{85}\text{Kr}$  also governs the  $^{88}\text{Sr}/^{86}\text{Sr}$  abundance ratio. More neutron capture at  $^{85}\text{Kr}$  leads to lower production of  $^{86}\text{Sr}$  and, thus, a higher  $^{88}\text{Sr}/^{86}\text{Sr}$  abundance ratio. The ratio has been measured in presolar mainstream



Original content from this work may be used under the terms of the [Creative Commons Attribution 4.0 licence](https://creativecommons.org/licenses/by/4.0/). Any further distribution of this work must maintain attribution to the author(s) and the title of the work, journal citation and DOI.



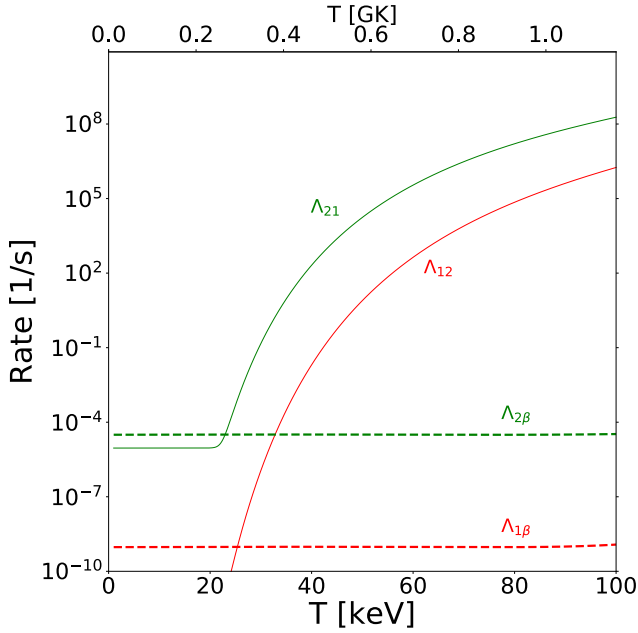


**Figure 2.**  $^{85}\text{Kr}$  effective transition rates (solid) and ensemble  $\beta$ -decay rates (dashed).

In this equation,  $f_{ij}$  is the comparative half-life (the contribution to the half-life that depends only on the square of the nuclear transition matrix element and physical constants), and  $f_{ij}$  is the phase-space integral that counts incoming and outgoing lepton momentum states. The G. M. Fuller et al. (1980) method incorporates results from N. Gove & M. Martin (1971) and B. A. Brown et al. (1978) with lepton blocking factors relevant to stellar interiors:

$$f_{ij} = \int_{m_e}^{Q_{ij}} \times \mathcal{E}_e^2 (Q_{ij} - \mathcal{E}_e)^2 G(+Z, \mathcal{E}_e) (1 - S_-) (1 - S_\nu) d\mathcal{E}_e. \quad (7)$$

Here,  $Q_{ij} \equiv \Delta E_{ij} = M_i - M_j + E_i - E_j$  is the total change in nuclear energy,  $\mathcal{E}_e = E_e + m_e$  is the total energy of the outgoing electron, the phase-space integral arguments are the total change in nuclear energy  $\Delta E_{ij} = E_j - E_i$  (rest mass plus excitation), the temperature  $T$ , and the electron chemical potential  $\mu_e$ . We computed the  $f_{ij}$  using the 64-point Gauss-Legendre quadrature for the portion of the ambient electron energy distribution with occupation probability  $F > 0.5$  ( $E < \mu_e$ ) and 64-point Gauss-Laguerre quadrature for the tails with  $F < 0.5$  ( $E > \mu_e$ ).

Following G. M. Fuller et al. (1980), we supplemented measured data by assuming  $\log(ft) = 5$  for unmeasured allowed weak transitions. For the sensitivity of weak transitions to  $\log(ft)$  values see S. Turkat et al. (2023). Figure 2 shows our computed ensemble transition rates and effective  $\beta$ -decay rates for the relevant rates in  $^{85}\text{Kr}$ .

Of course, using  $\log(ft) = 5$  for unmeasured transitions is only a very rough approximation, and we show in Figure 3 the ratio of the  $\beta$ -decay rates computed using the supplemented data to the rates using only the measured  $\log(ft)$  values. We find that below  $T \sim 80$  keV, the inclusion of  $\beta$  decays for excited states beyond the isomer does not affect the ensemble  $\beta$ -decay rates; this agrees with the findings of K. Takahashi & K. Yokoi (1987). Furthermore, our low-temperature ensemble

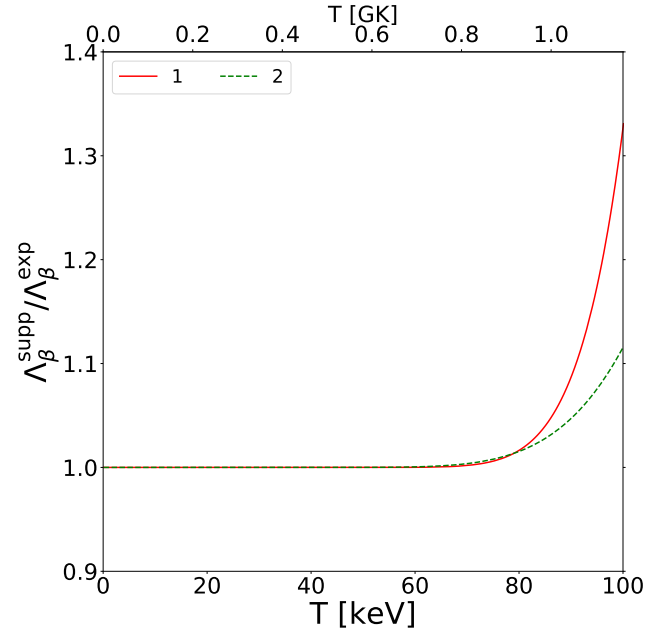


**Figure 3.** Ratio of  $^{85}\text{Kr}$   $\beta$ -decay rates computed using supplemented experimental data to rates computed using experimental data alone. Supplemented data assumes  $\log(ft) = 5$  for allowed transitions. The solid red line shows the ground state ensemble, and the dashed green line shows the isomer ensemble.

decay rates correspond to the ground state and isomer decay rates reported by the NNDC (B. Singh & J. Chen 2014).

Another key quantity required for nucleosynthesis network calculations is the partition function  $G_A(T)$ , which measures the multiplicity for ensemble  $A$  at temperature  $T$ . In the network calculations presented here, the partition functions are required to compute reverse reaction rates from the corresponding forward reaction rate from detailed balance. Again following S. S. Gupta & B. S. Meyer (2001), we construct the  $G_A$  using the weights  $w_{iA}$  and the spin  $J_A$ :

$$G_A = (2J_A + 1) \sum_i w_{iA}. \quad (8)$$

Because we compute the  $w_{iA}$  using ratios of transition rates rather than with explicit consideration of spins and energies, we may be assured that our effective transition rates, ensemble  $\beta$ -decay rates, and partition functions are all calculated self-consistently. We show the ensemble partition functions in Figure 4. Note that up to  $T = 100$  keV, they increase by less than 1% since the levels beyond the isomer are not populated at these temperatures.

More advanced shell models that incorporate microscopic physics have been developed to calculate  $\beta$ -decay rates in stellar environments, as demonstrated in K. Langanke & G. Martinez-Pinedo (2000) and J. Nabi & H. Klapdor-Kleingrothaus (2004). While these methods extend beyond the scope of the current study, they should be considered for inclusion in future studies.

### 3. Building Intuition

In this section, we explore the interplay between the ground and isomeric states of  $^{85}\text{Kr}$  to understand how an equilibrium between the two develops, if at all. To do so, we allow the isotope to evolve between the ground and isomeric states in an

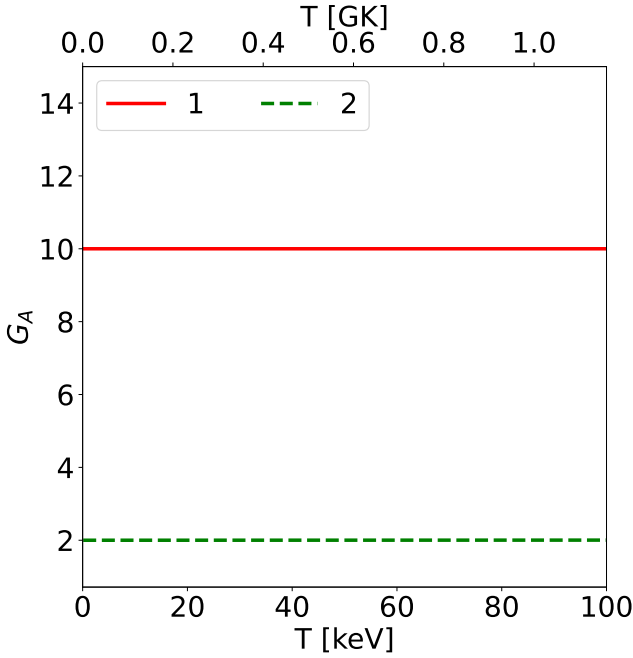


**Figure 4.**  $^{85}\text{Kr}$  ensemble partition functions. The solid red line shows the ground state ensemble, and the dashed green line shows the isomer ensemble.

isolated fluctuating thermal bath and focus on changes in the isomeric mass fraction. We implement a simple two-level model to evolve the system of equations. The mass fraction of the first state,  $X_1$ , is governed by the equation

$$\frac{dX_1}{dt} = \Lambda_{21}X_2 - \Lambda_{12}X_1, \quad (9)$$

while the mass fraction  $X_2$  of the second state is governed by

$$\frac{dX_2}{dt} = \Lambda_{12}X_1 - \Lambda_{21}X_2. \quad (10)$$

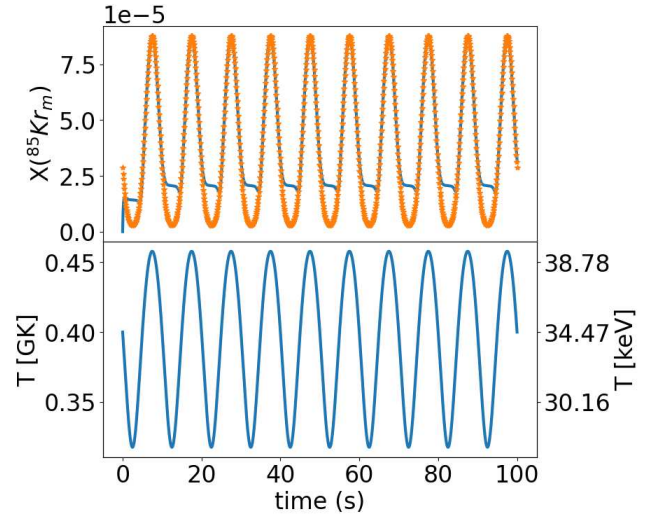
The  $\Lambda$ 's, the appropriate transition rates between the two states, are taken from Figure 2. A sinusoidal temperature profile was generated to mimic the temperature fluctuations that occur during the thermal pulsations of late-stage evolution of low- and intermediate-mass stars, with the maximum and the minimum in  $s$ -process temperature range. The system has initial conditions of  $X_1 = 1.0$  and  $X_2 = 0.0$ . An equilibrium value for  $X_2$  as a function of temperature can be calculated via Boltzmann statistics:

$$X_{2\text{eq}} = G_2(T_9) \frac{e^{-11.605 \times Q/T_9}}{G_1(T_9) + G_2(T_9) \times e^{-11.605 \times Q/T_9}}. \quad (11)$$

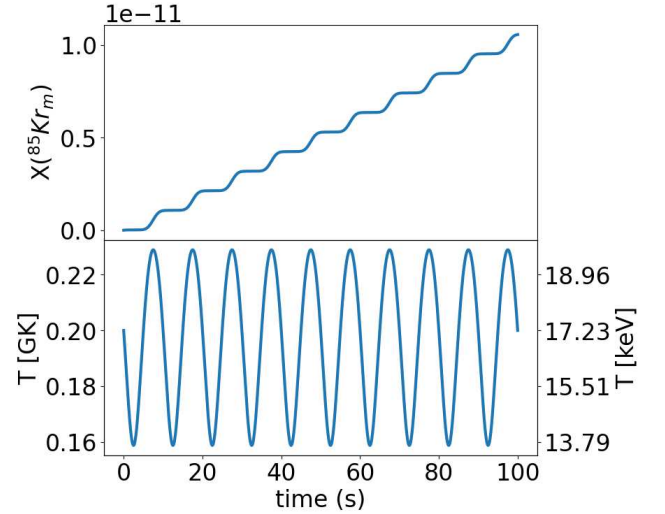
$Q$  here is the difference in mass excess of the ground and isomeric states and is equal to 0.305 MeV, and the 11.605 factor is the inverse Boltzmann constant in eV/K scaled to account for the units of  $Q$  and  $T_9$ .

Figure 5 illustrates a “breakaway” behavior. Ideally, the mass fraction would evolve alongside the equilibrium value, but as the temperature drops, the decay rate to the ground state falls so low the mass fraction plateaus. As the temperature rises again, the rate rises enough so the mass fraction now returns to the equilibrium value. The network maintains equilibrium until the temperature again drops to a low value.

Running the same calculation again but with a lower temperature leads to slow excitation and deexcitation rates,



**Figure 5.** Mass fraction time evolution of the isomeric state of  $^{85}\text{Kr}$  as calculated by the network compared to the equilibrium mass fraction in blue and orange, respectively, in the top panel. The bottom panel is the temperature profile as a function of time.



**Figure 6.** Mass fraction time evolution of the isomeric  $^{85}\text{Kr}$  as determined by the network in the top panel. The equilibrium evolution is not graphed here since it is orders of magnitude larger than the network calculation. The bottom panel is the temperature profile.

reflected in Figure 6 by the small amount of mass that gets “pumped” up from the ground state to the isomeric state each cycle. Despite the higher deexcitation rate, as seen in Figure 2, the temperature fluctuation timescale is much faster, allowing the isomeric mass fraction to level off during the temperature drop. As the temperature rises, the excitation rises, adding to the isomeric mass fraction and leading to the “stair-step” behavior.

Despite the clear differences between these simplistic profiles and real stellar environments, the simple model clearly illustrates how the isomer’s mass fraction gets populated and destroyed as the temperature fluctuates relative to the equilibration temperature.

#### 4. Stellar Environments

Two sites provide the necessary conditions for the  $s$ -process to occur. The first site is the Helium shell of low- and



intermediate-mass stars in their thermal pulsing asymptotic giant branch (TP-AGB) phase. The second is in the core and shells of massive stars, which have achieved core helium burning and beyond. The process yields, pathways, and extent are affected by the star's capability to generate neutrons and the amount of heavy seed nuclei, such as  $^{56}\text{Fe}$ , the star accreted during its formation.

Each site has different  $s$ -process yields and endpoints. Fittings done by D. D. Clayton & M. Rassbach (1967) and D. D. Clayton & R. A. Ward (1974) on the  $\sigma N$  curve for the solar system show that the  $s$ -process yields fall into two components. The main component yields nuclei in the mass range of  $90 < A < 210$ , while the weak component yields nuclei with masses around  $A \sim 90$ . The main branch  $s$ -process nucleosynthesis occurs in TP-AGB stars with  $^{13}\text{C}$  as its neutron source. It is created during the third dredge-up (R. Kippenhahn et al. 1990) and produces neutrons via  $^{13}\text{C}(\alpha, n)^{16}\text{O}$ . The weak  $s$ -process branch occurs during and beyond core Helium burning in massive stars,  $M \gtrsim 12 M_{\odot}$ . Despite the presence of  $^{13}\text{C}$ , its contribution to the neutron flux is overshadowed by  $^{22}\text{Ne}$  via  $^{22}\text{Ne}(\alpha, n)^{25}\text{Mg}$ . Since the neutron flux range for the  $s$ -process is between  $10^5$  and  $10^{11} \text{ cm}^{-2} \text{ s}^{-1}$ , it cannot produce heavy radioactive isotopes such as thorium, uranium, and plutonium. Heavy radioactive isotopes are exclusively produced in the rapid neutron-capture process (E. M. Burbidge et al. 1957; T. Kajino et al. 2019; J. J. Cowan et al. 2021; E. M. Holmbeck et al. 2023). The  $s$ -process, in contrast, terminates in a bismuth, lead, and polonium loop (U. Ratzel et al. 2004).

We performed our nucleosynthesis calculations with the Webnucleo reaction network code (B. Meyer 2013). This network is built on top of the network library libnucnet (B. S. Meyer & D. C. Adams 2007), which can include an arbitrary number of independent ensembles of isomeric states for each nuclear species. To follow  $s$ -process nucleosynthesis, we used a version of the code that allows the network to follow a prescribed abundance for a particular species (in this case, the neutron abundance). To use this version of the code for the  $^{85}\text{Kr}$  isomer problem, key inputs are required. The first is the set of nuclear network data (V2.2 of the REACLIB database R. H. Cyburt et al. 2010) supplemented by the reaction rates involving both the ground and isomeric states of  $^{85}\text{Kr}$ , all of which are illustrated in Figure 7. The second input required is the neutron number density profile as a function of temperature and time, henceforth known as the trajectory. To build the trajectory, a  $2 M_{\odot}$  stellar model with metallicity  $Z = Z_{\odot}$  was evolved from zero-age main sequence with Modules for Experiments in Stellar Astrophysics (MESA; B. Paxton et al. 2011, 2013, 2015, 2018, 2019; A. S. Jermyn et al. 2023) to the start of the TP-AGB phase. A snippet of the trajectory can be seen in Figure 8.

An open-source TP-AGB trajectory building tool<sup>7</sup> (J. Tannous 2025) was inspired by the elliptical attributes featured in this snippet. The tool is designed to construct a full trajectory utilizing an elliptical approximation that evolves to next thermal pulse without the need to run lengthy and complicated stellar models. The third and final input required is the isotopic composition of the zone. Our calculations used solar abundances compiled by K. Lodders (2003). The results of our single-zone calculations are discussed in the next section.

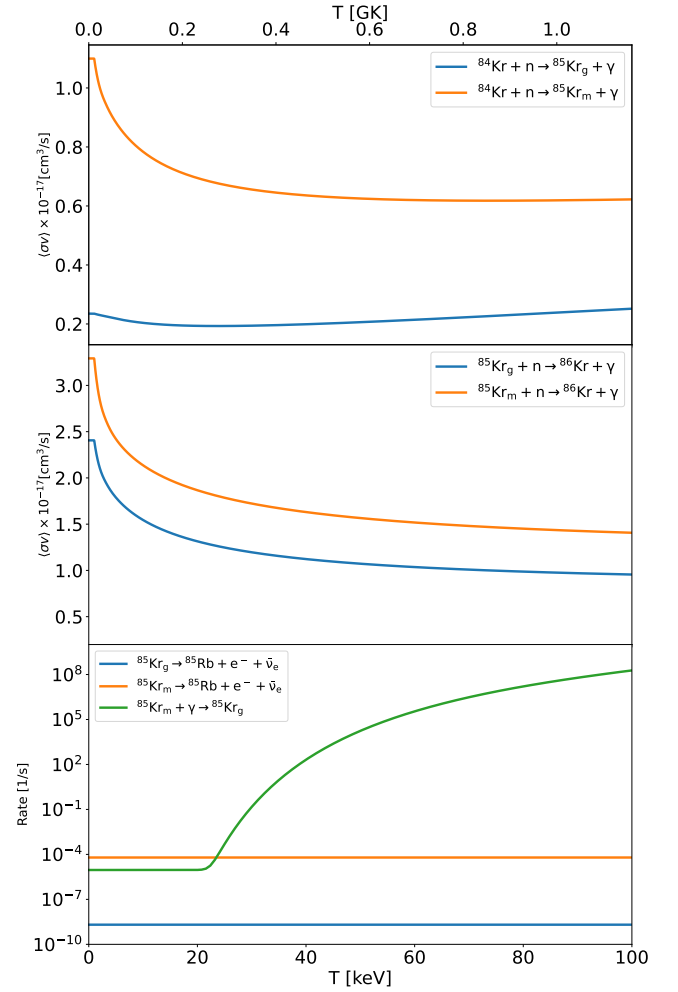


**Figure 7.** Relevant rates involving the isomeric and ground states of  $^{85}\text{Kr}$ . The top two graphs show the neutron cross-section rates in and out of  $^{85}\text{Kr}$ , respectively. They show that the dominant pathway in and out of  $^{85}\text{Kr}$  via neutron capture is through the isomer. To get the actual neutron-capture rate, one must multiply the thermally averaged cross section  $\langle\sigma v\rangle$  by the neutron number density,  $n_n$ . The bottom graph contains the  $\beta$ -decay and internal transition rate of both states of  $^{85}\text{Kr}$ . For temperature  $T_0$  less than about 0.27, the  $^{85}\text{Kr}$  isomer will  $\beta$ -decay rather than equilibrate with ground state.

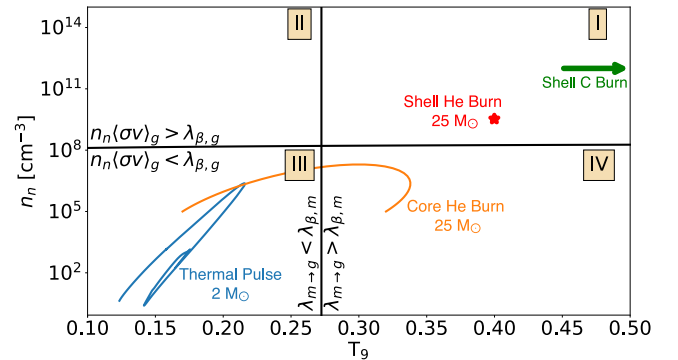


**Figure 8.** Trajectories in the temperature–number density plane depicting where the  $s$ -process occurs. The blue curve shows the 10th thermal pulse of a  $2 M_{\odot}$  TP-AGB MESA model from the test suite, the orange curve shows core He burning in a  $25 M_{\odot}$  model (M. F. El Eid et al. 2007), the red symbol marks shell He burning in the  $25 M_{\odot}$  model, and the green arrow indicates the direction to shell C burning.

<sup>7</sup> [https://github.com/jaadt7/elliptical\\_trajectory](https://github.com/jaadt7/elliptical_trajectory)

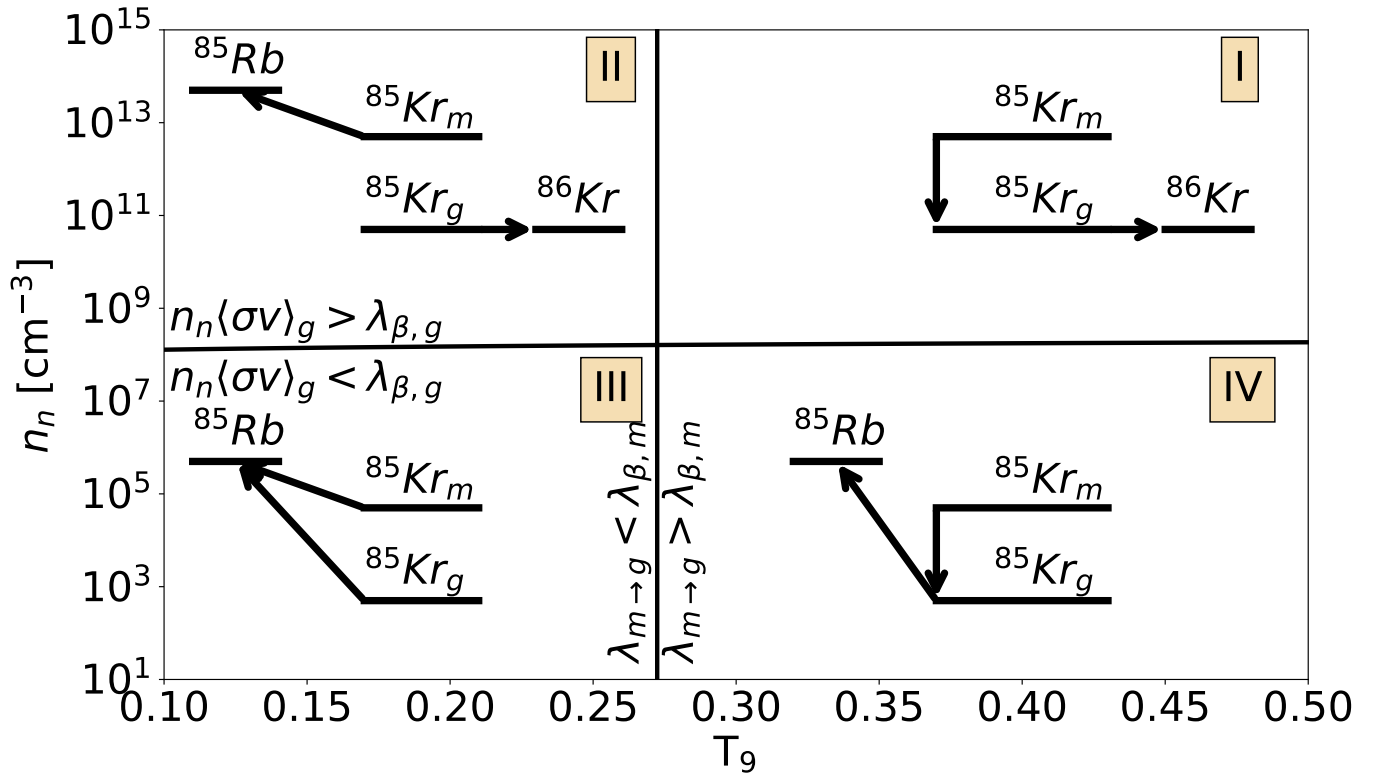


**Figure 9.** The preferential reactions that occur between the isomeric state and the ground state at a given region of  $n_n$  and  $T_9$ . For added context, the beta-decay half-lives are 4.48 hr and 10.739 yr for the isomer and ground state, respectively.

### 5. Results

The branching behavior of  $^{85}\text{Kr}$  in an  $s$ -process environment is governed principally by the neutron number density  $n_n$  and the temperature  $T_9$ . Figure 8 shows a grid of  $n_n$  and  $T_9$  with typical  $s$ -process conditions in astrophysical environments.

The vertical line in the grid is the temperature at which the decay rate from the isomer to the ground state is equal to the  $\beta$ -decay rate of the isomer, while the horizontal line is determined from the neutron number density required for the neutron-capture rate to be equal to the  $\beta$ -decay rate for the ground state. Each quadrant in the grid represents a nuclear transmutation path within an astrophysical setting determined by each grid's extent. Uncertainties in the isomerization rate will affect the grid by shifting or broadening the vertical line.

To understand  $s$ -process flow in each quadrant, we run simple constant trajectories, i.e., trajectories of constant  $n_n$  and  $T_9$ , in each quadrant, the results of which are summarized in Figure 9. Each quadrant has its own distinct flow pattern. Quadrants I and IV have high enough temperatures that thermalize the isomer with the ground state. Thus, branching to  $^{86}\text{Kr}$  or  $\beta$ -decaying to  $^{85}\text{Rb}$  will all occur from the ground state and depends on  $n_n$ . Quadrants II and III's temperature is low enough that  $^{85}\text{Kr}$  is considered to be an astromer. The low  $n_n$  of quadrant III allows for the  $\beta$ -decay of both states into  $^{85}\text{Rb}$ , but each at its own half-life. Most intriguing is quadrant II, where the isomer seems completely disconnected from the ground state. The high  $n_n$  and longer half-life allows what little amount of  $^{85}\text{Kr}$  synthesized from  $^{84}\text{Kr} + n \rightarrow ^{85}\text{Kr} + \gamma$  in the ground state to branch over to  $^{86}\text{Kr}$ , while the amount synthesized to the isomeric state  $\beta$ -decays to  $^{85}\text{Rb}$ .

As Figure 8 depicts, trajectories need not be confined to a single quadrant, as illustrated by the trajectory in the Helium

core of the  $25 M_\odot$  star crossing from quadrants III to IV. Some AGB and super-AGB stars have trajectories crossing over quadrants II, III, and IV. To simplify the study, we analyze the effects of the astromer on main branch  $s$ -process by considering the conditions of a  $2 M_\odot$  undergoing TP-AGB. We also study the effect the astromer has on the weak branch by considering the conditions of  $25 M_\odot$  undergoing core Helium burning. A full tutorial on how to construct trajectories, run network calculations, and postprocessing is housed on Open Science Framework (J. Tannous & B. S. Meyer 2023).

$s$ -process yields from a real star arise from a variety of ejecta with differing exposures. To get a better understanding of the role of the  $^{85}\text{Kr}$  astromer on actual abundance yields, we average our abundances over a distribution of exposures:

$$Y_i(\tau_0) = \int_0^\infty Y_i(\tau) \rho(\tau, \tau_0) d\tau, \quad (12)$$

where the subscript  $i$  denotes the species and the distribution of exposures  $\rho(\tau)$  gives the fraction of nuclei that have seen exposure between  $\tau$  and  $\tau + d\tau$ . In Equation (12),  $\tau_0$  is a parameter (or set of parameters) characterizing the distribution. The distribution is normalized such that

$$\int_0^\infty \rho(\tau, \tau_0) d\tau = 1. \quad (13)$$

We choose to evaluate our results by considering an exponential distribution of exposures given by

$$\rho(\tau, \tau_0) = \frac{1}{\tau_0} e^{-\tau/\tau_0}. \quad (14)$$

The quantity  $\tau_0$  is the average exposure in the exponential distribution. D. D. Clayton & M. Rassbach (1967) and D. D. Clayton & R. A. Ward (1974) determined that the solar

system's  $s$ -process abundance pattern is well described by three distinct exponential distributions of neutron exposures. One distribution, with  $\tau_0 \approx 0.30 \text{ mb}^{-1}$ , produces most of the nuclei in the mass range  $90 < A < 204$ . This is the main component. Another exposure, with  $\tau_0 \approx 0.06 \text{ mb}^{-1}$ , contributes to the  $A \lesssim 90$   $s$ -nuclei abundances. This weak component is required in order to explain the  $\sigma N$  curve around  $A \approx 90$ . These two distributions indicate that two separate sites contributed to the abundance of solar  $s$ -nuclei. Finally, a strong component, with  $\tau_0 \approx 7.0 \text{ mb}^{-1}$ , may be necessary to explain the abundances of the  $A = 204\text{--}209$  nuclei. A possible explanation of this component is that lower-metallicity AGB stars reach higher exposures, giving an overall nonexponential distribution at large  $\tau$ . There is probably no need for a separate site for the strong component of the  $s$ -process (R. Gallino et al. 1998).

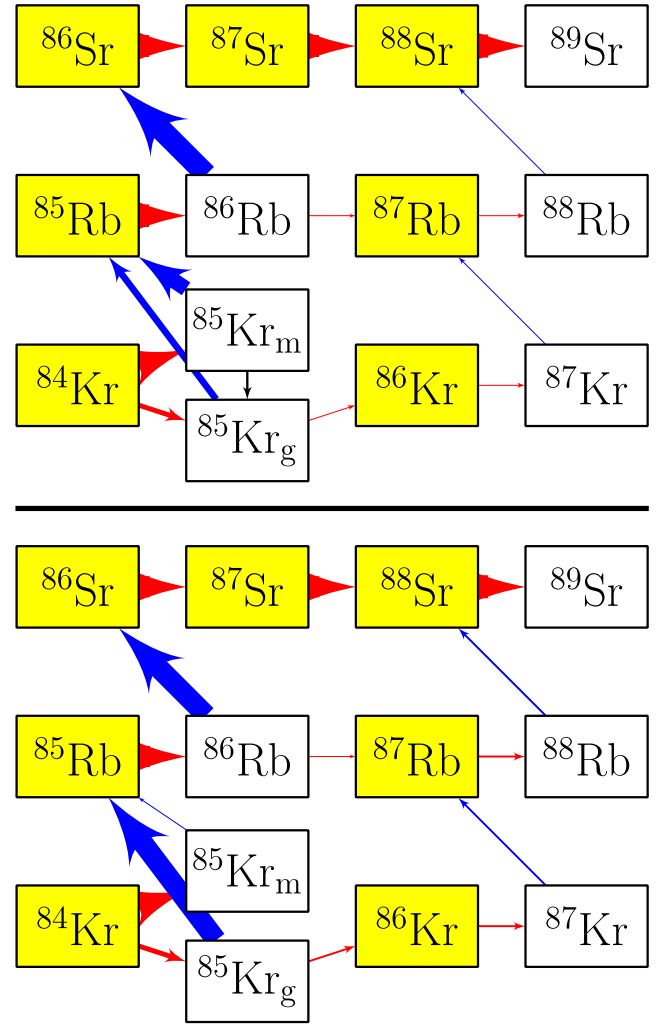
### 5.1. Main Component $s$ -process

We consider the  $2 M_\odot$  case because its trajectory lives solely in quadrant III. To infer any effect due to the isomer's inclusion, we execute single-zone calculations under two conditions: a reference condition, where the nuclear network operates with the rates calculated in Section 2, and an equilibrated condition, where we modify the  $^{85}\text{Kr}_m + \gamma \rightarrow ^{85}\text{Kr}_g$  rate by a factor of  $10^{10}$  at all temperatures to enforce equilibration with the ground state. The trajectory itself consists of 25 pulses in the TP-AGB phase.

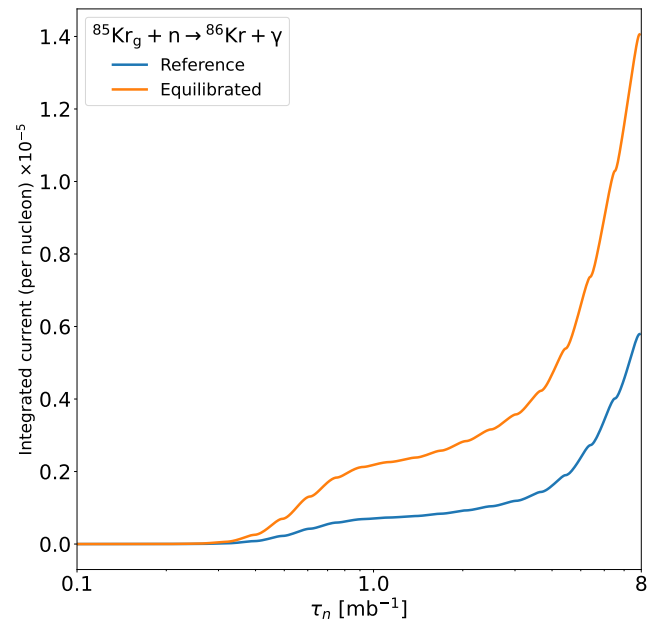
To study the branching at  $^{85}\text{Kr}$  with and without isomeric equilibration, it is useful to visualize the  $s$ -process flow between the two cases. Figure 10 depicts the integrated current flow each case undergoes. In both, the major pathway to the strontium isotopic chain is via the  $\beta$ -decays of  $^{85}\text{Kr}$ , both states, and  $^{86}\text{Rb}$ . In the equilibrated case, the figure does not show any current from  $^{85}\text{Kr}_m$  to  $^{85}\text{Kr}_g$ . Our integrated current code does not properly account for this because it uses abundances after successful solution of the network equations at each timestep. At such a point, the ground state and the isomer are essentially equilibrated and the computed net current is zero; hence, the lack of a computed net current for the deexcitation of the isomer in the figure. Since, in this calculation, the ground and isomer are always extremely close to being equilibrated, flow into  $^{85}\text{Kr}_m$  is effectively redistributed instantaneously into a Boltzmann distribution among the  $^{85}\text{Kr}$  levels, and that equilibrium distribution is heavily dominated by  $^{85}\text{Kr}_g$ . Thus, in this case, it is no longer necessary to distinguish between the ground and isomer, and one can consider  $^{85}\text{Kr}$  to be fully equilibrated internally. For other reactions in the network, such as  $^{84}\text{Kr} + n \rightarrow ^{85}\text{Kr}_m + \gamma$ , the reverse reaction is negligible in  $s$ -process conditions, and our code correctly computes the integrated current. Of course, other nuclides in the network are always considered to be fully equilibrated internally. At first glance, it would seem that  $^{85}\text{Kr}$  does not behave as an astromer in this quadrant.

Figure 11 shows the difference of integrated current for the reaction  $^{85}\text{Kr}_g + n \rightarrow ^{86}\text{Kr} + \gamma$ . Essentially, the longer  $\beta$  half-life in the ground state increases the probability of branching over. Increased abundance of  $^{85}\text{Kr}_g$  due to the forced equilibration further increases the probability, reflected in the current. This contrast cements the astromeric status of  $^{85}\text{Kr}$  in this quadrant.

Isotopic abundance and ratios of  $^{87}\text{Rb}$  and  $^{88}\text{Sr}/^{86}\text{Sr}$  support this claim. Starting with  $^{87}\text{Rb}$ , Figure 12 depicts its abundance per nucleon as a function of neutron exposure,  $\tau_n$ . The



**Figure 10.** Current diagrams depicting the dominant flow of  $s$ -process nucleosynthesis centered around  $^{85}\text{Kr}$ . The top chart represents the reference case, while the bottom represents the equilibrated case.



**Figure 11.** The integrated current of the branching reaction from the ground state of  $^{85}\text{Kr}$ .

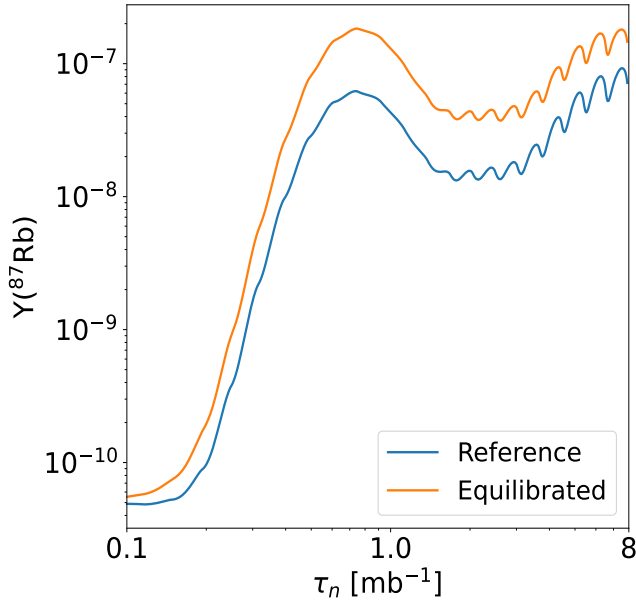


**Figure 12.** Comparison of  $^{87}\text{Rb}$  abundances from single-zone calculation with  $^{85}\text{Kr}$  equilibrated vs. nonequilibrated.

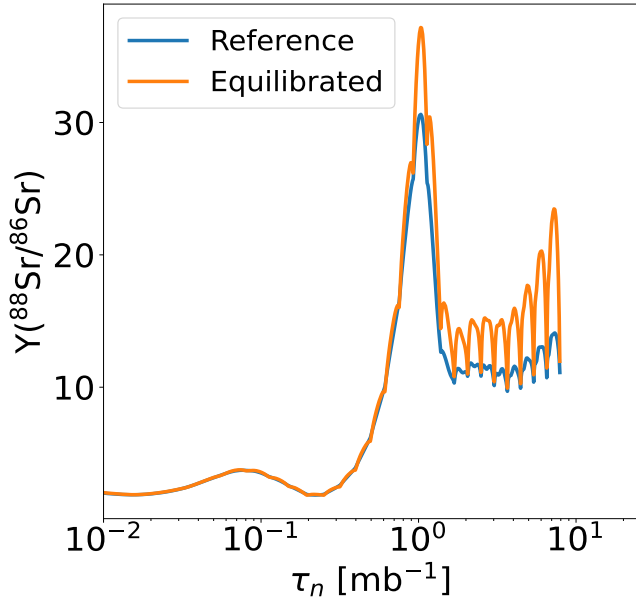


**Figure 13.** The abundance ratio of  $^{88}\text{Sr}$  to  $^{86}\text{Sr}$  as a function of neutron exposure.

abundance builds up as  $s$ -process flow brings neighboring isotopes up to  $^{87}\text{Rb}$ . Further exposure causes the flow to pass beyond  $^{87}\text{Rb}$  to higher-mass nuclei but is built up again as the  $s$ -process brings isotopes up to  $^{87}\text{Rb}$  from  $^{56}\text{Fe}$ .  $^{85}\text{Kr}$  is not equilibrated in the reference case leading to a difference in the abundance starting with an exposure as low as  $\sim 0.03 \text{ mb}^{-1}$ . This is due to the combination of the isomeric  $^{85}\text{Kr}$   $\beta$ -decaying on a much shorter timescale than its ground state and the low neutron number density of the trajectory as a whole, reducing the synthesis of  $^{87}\text{Rb}$  by a factor of a few. An interesting feature is the ridge-like features shown in the graph, which correspond to the fluctuations in temperature and neutron number density in time along the trajectory.

In the  $^{88}\text{Sr}/^{86}\text{Sr}$  ratio case, Figure 13, we see only a clear difference for exposures greater than  $1 \text{ mb}^{-1}$ . Just as with the

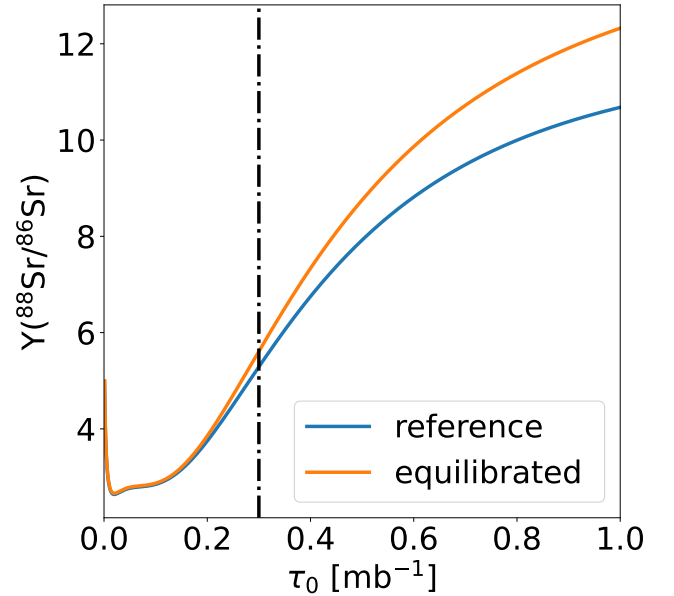
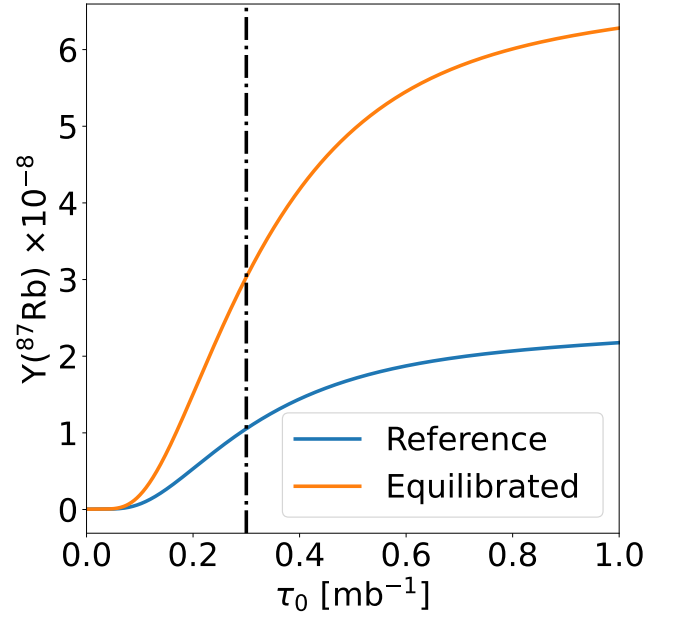


**Figure 14.** Isotopic abundances averaged over an exponential distribution of neutron exposure. The dashed vertical line indicates the average exposure for the main component of the  $s$ -process, a  $\tau_0$  of  $0.3 \text{ mb}^{-1}$ .

$^{87}\text{Rb}$  case, the first bump is the abundance buildup up as  $s$ -process flow brings neighboring isotopes up the strontium isotopic chain and further exposure brings the flow up from  $^{56}\text{Fe}$ . As the exposure grows beyond  $\tau_n = 1 \text{ mb}^{-1}$ , the equilibrated case shows a higher ratio during the climb of the  $n_n$  but returns to the same value as the reference case during the drop.

The averaged yields illustrated in Figure 14 show a reduction in yields by a factor of a few to a factor of several. Yields in  $^{87}\text{Rb}$  show deviation for exposures lower than the weak  $s$ -process exposure, while the strontium ratio shows major deviation after the main  $s$ -process exposure.

In summary, incorporating isomeric  $^{85}\text{Kr}$  in AGB stars is expected to decrease the overall yield of  $^{87}\text{Rb}$ . Specifically as the weak branch exposure gets accumulated, the yield reduces from  $5.306 \times 10^{-11}$  in the equilibrated case to  $5.099 \times 10^{-11}$



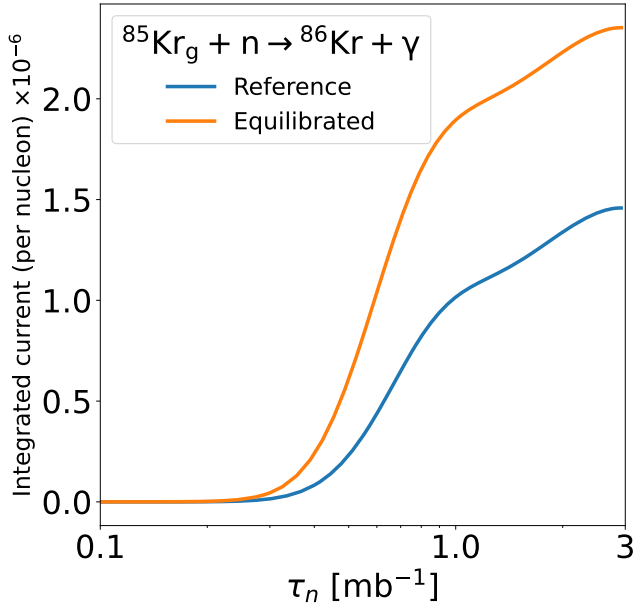


**Figure 15.** The integrated current of the branching reaction from the ground state of  $^{85}\text{Kr}$ .

in the reference case. Additionally, the yield decreases from  $3.972 \times 10^{-9}$  in the equilibrated case to  $1.651 \times 10^{-9}$  in the reference case by the time the main branch exposure gets accumulated. This adjustment also results in an increase in  $^{86}\text{Sr}$ , leading to a lower  $^{88}\text{Sr}/^{86}\text{Sr}$  ratio during exposures beyond the main branch  $s$ -process.

### 5.2. Weak Component $s$ -process

We construct a trajectory, the orange curve in Figure 8, for a  $25 M_{\odot}$  star undergoing core Helium burning based on the work done by M. F. El Eid et al. (2007). Such a trajectory allows us to explore how the isomeric state of  $^{85}\text{Kr}$  plays a role in the weak branch of the  $s$ -process. Studying this trajectory also yields insight into the behavior of the  $s$ -process network as the trajectory passes from one quadrant into another. Calculations were carried out in the same fashion to the TP-AGB star for main branch case.

The crossover from quadrant III into IV can be seen in the integrated current shown in Figure 15. While the trajectory is in quadrant III, the reference case deviates from the equilibrated case at a fixed rate. As soon as the trajectory crosses over into quadrant IV, at  $\tau_n \sim 0.9 \text{ mb}^{-1}$ , the currents now run in parallel, indicating the complete equilibration of  $^{85}\text{Kr}$ . This results from  $^{85}\text{Kr}$  forfeiting its astromer status as the isotope thermalizes when the trajectory crosses into quadrant IV at  $T_9 = 0.273$ .

In terms of isotopic yields, the trajectory leaves little room for change. Figure 16 shows that there is a common feature between the rubidium and strontium ratios. Both display deviations in their abundances relative to the fully equilibrated case at low exposures in quadrant III, which later converge upon crossing into quadrant IV.  $^{87}\text{Rb}$  abundance in the reference case deviates from the equilibrated case by a factor of a few, just as it does in the main branch at low exposures. As the exposure grows while the trajectory crosses into quadrant IV, both cases converge since  $^{85}\text{Kr}$  will equilibrate in

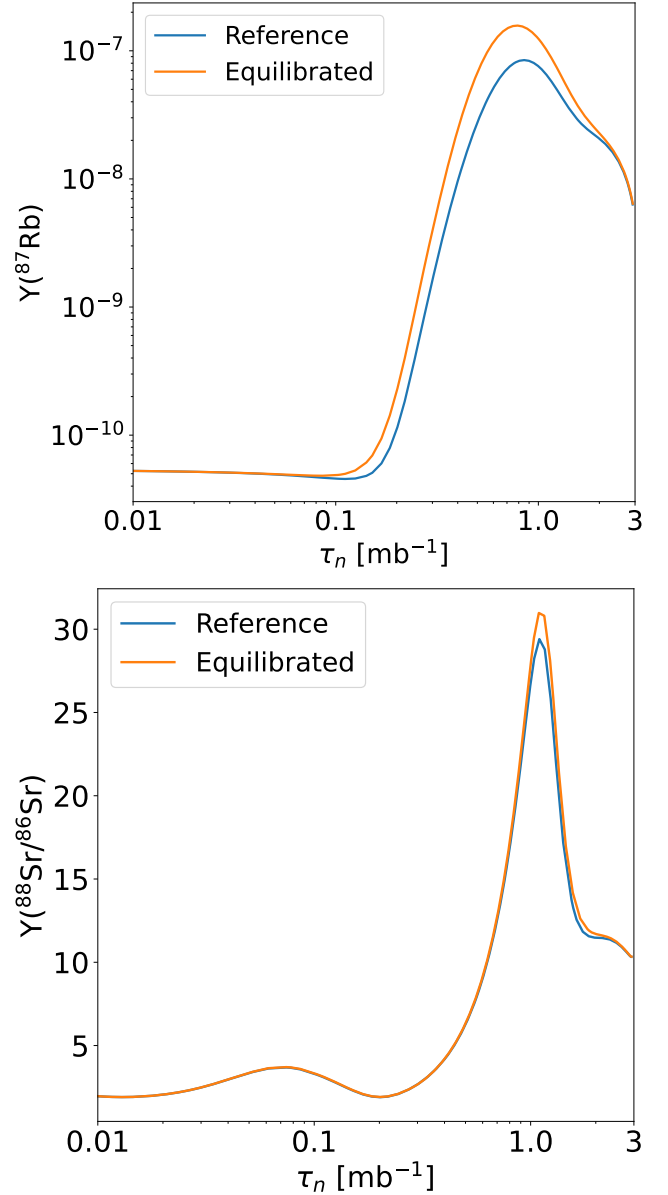


**Figure 16.**  $^{87}\text{Rb}$  abundance and  $^{88}\text{Sr}/^{86}\text{Sr}$  abundance ratio both as a function of exposure during core helium burning of the  $25 M_{\odot}$  star.

the reference case.  $^{88}\text{Sr}/^{86}\text{Sr}$  shows little to no deviation in this trajectory at all. A minor shift is visible at peak abundance with  $\tau_n \sim 0.5 \text{ mb}^{-1}$ .

Figure 17 shows there is no change in the strontium ratio over integration over exposures until characteristic exposure is well beyond that typical of the main branch, thus indicating no astromeric behavior.  $^{87}\text{Rb}$  however indicates a clear shift in abundance yields just beyond the weak branch characteristic exposure. It can be explained via the network building up abundances based on the existing isotopes from the solar metallicity and deviating at the exposure  $\sim 0.06 \text{ mb}^{-1}$ , since the trajectory is still in quadrant III where  $^{85}\text{Kr}$  is an astromer.

Astromer  $^{85}\text{Kr}$  has no major effect on strontium production in massive stars but still affects  $^{87}\text{Rb}$ . We infer that the  $^{87}\text{Rb}$  abundance will be reduced in the massive star case by a factor of  $\sim 2$  for  $\tau_0$  somewhat greater than the  $0.06 \text{ mb}^{-1}$  inferred from the solar abundances, as apparent from Figure 17.

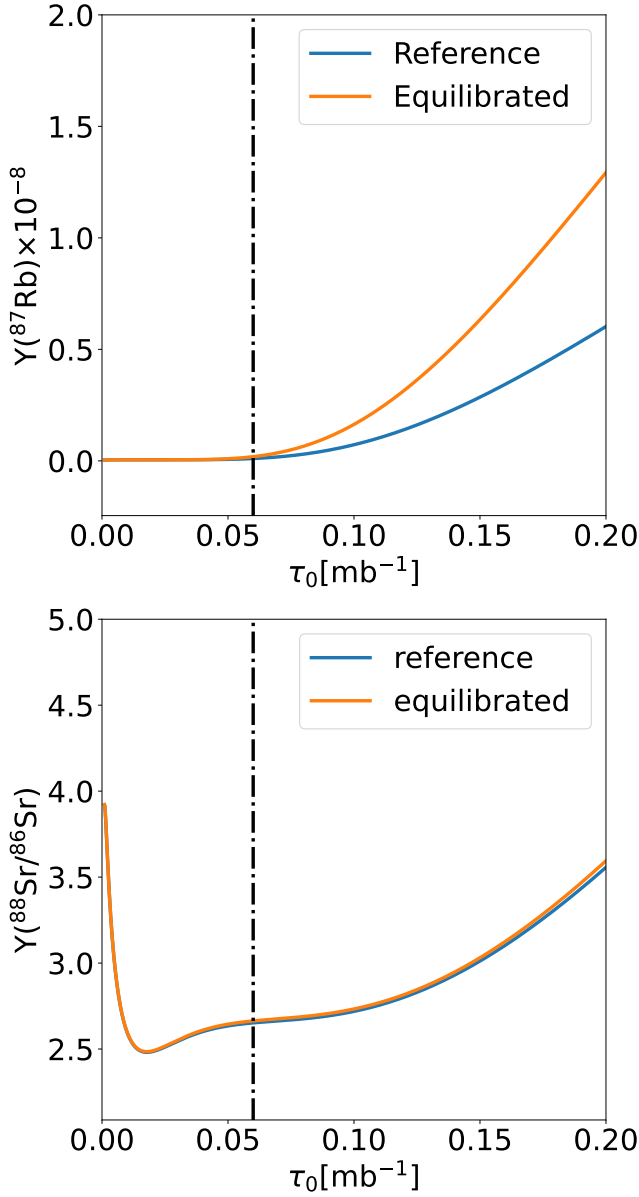


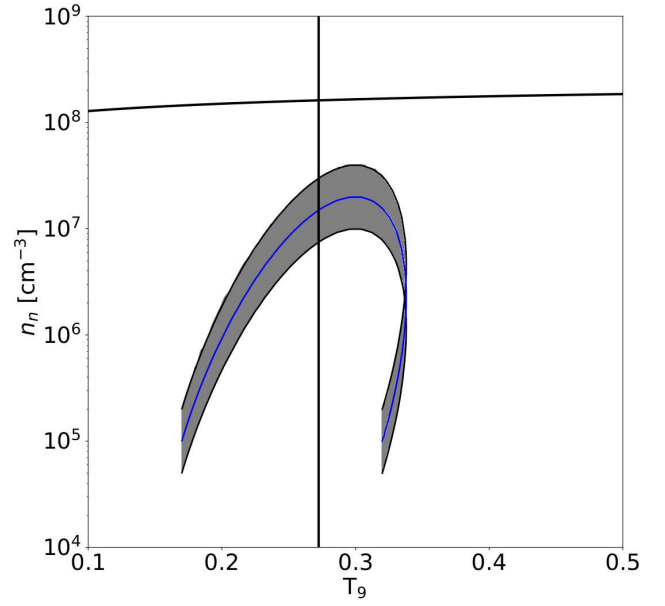
**Figure 17.** Isotopic abundances averaged over an exponential distribution of neutron exposure. The dashed vertical line indicates the average exposure for the weak component of the  $s$ -process, a  $\tau_0$  of  $0.06 \text{ mb}^{-1}$ .

### 5.3. Trajectory Uncertainty

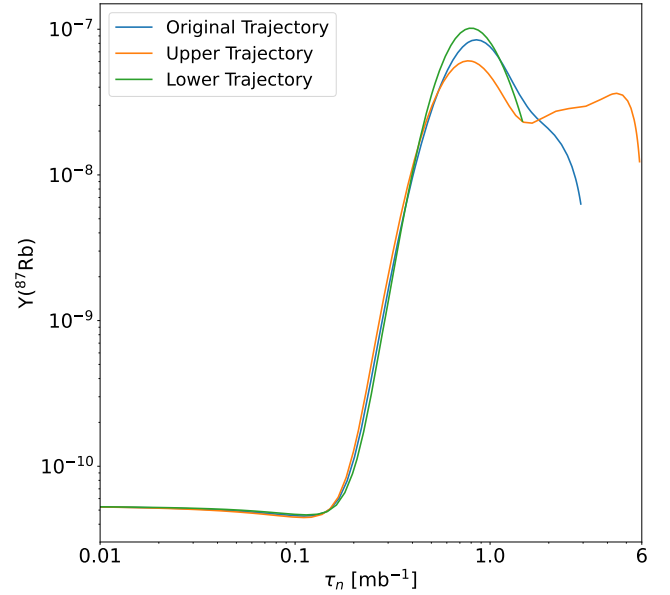
As we mentioned before, the trajectories built were based on specific models and conditions. Stellar models at different mass locations, or different metallicity, mass, and input physics will lead to modified trajectories.

Figure 18 is the same grid as in Figures 8 and 9, modified to focus on the core He burning trajectory. Our chosen trajectory for the weak branch  $s$ -process calculations, in blue, is situated in the uncertainty band where fluctuations in the trajectory are expected to be.

To quantify the effect the different trajectories may have, we chose the bounding trajectories and compared the  $^{87}\text{Rb}$  abundance with the original trajectory. Minor variations can be noted in Figure 19 at exposures of  $\sim 0.05 \text{ mb}^{-1}$ . At higher exposures, the trends diverge. First, the extent of each trajectory in terms of neutron exposure is in line with expectations that are based on the difference in peak  $n_n$  of



**Figure 18.** The blue curve shows core He burning in a  $25 M_{\odot}$  model (M. F. El Eid et al. 2007) as before, embedded in the uncertainty band.



**Figure 19.**  $^{87}\text{Rb}$  abundance as a function of neutron exposure for the upper, original, and lower trajectories.

each trajectory. Second, the lower trajectory has built up the highest peak abundance of  $^{87}\text{Rb}$ . This is due to the overall lower  $n_n$  of the trajectory, which diminishes the network's ability to neutron capture out of  $^{87}\text{Rb}$ , thus building up its abundance until the flux is high enough to capture out. Most interestingly, and unexpectedly, the upper trajectory shows a double-hump feature. The first hump is the buildup from the existing neighboring isotopes based on the metallicity and starts to deplete via neutron capture in such a high  $n_n$  scenario. By the time the exposure reaches  $\sim 11 \text{ mb}^{-1}$ , the isotope buildup catches up and leads to the secondary hump. This small study was done to showcase the effect a single order-of-magnitude variation in the trajectory up or down may have on the overall abundance pattern.

## 6. Conclusions




We presented calculations of  $s$ -process nucleosynthesis that fully incorporate the effect of the  $^{85}\text{Kr}$  astromer. We showed that proper inclusion of the effect of the  $^{85}\text{Kr}$  astromer is important for predicting the  $s$ -process yield of  $^{87}\text{Rb}$ , an important cosmochronometer. The  $s$ -process abundance ratio  $^{88}\text{Sr}/^{86}\text{Sr}$  ratio, which can be measured in mainstream presolar SiC grains, is not significantly affected in the conditions we studied because the  $s$ -process flow through  $^{85}\text{Kr}$  is dominated by beta decay. Nevertheless, for  $s$ -process environments attaining conditions in quadrant II in Figure 8, proper inclusion of the  $^{85}\text{Kr}$  isomeric state will be essential for accurate predictions of this ratio, since, in this case, neutron-capture flow from the ground state will dominate the beta decay but the isomer will have the opposite behavior.

## Acknowledgments

J.T. and B.S.M. were supported in part by NASA grant 80NSSC20K0338. A.C., G.W.M., and M.R.M. were supported by the US Department of Energy through the Los Alamos National Laboratory. Los Alamos National Laboratory is operated by Triad National Security, LLC, for the National Nuclear Security Administration of U.S. Department of Energy (Contract No. 89233218CNA000001). M.R.M. acknowledges support from the Laboratory Directed Research and Development program of Los Alamos National Laboratory under project number 20230052ER and from the Directed Asymmetric Network Graphs for Research (DANGR) initiative at Los Alamos. A.C. acknowledges support from the Laboratory Directed Research and Development program of Los Alamos National Laboratory under project 20230052ER. J.T. acknowledges the feedback and useful comments provided by Toshihiko Kawano on the manuscript.

*Software:* Elliptical Trajectory Builder (J. Tannous 2025, [https://github.com/jaadt7/elliptical\\_trajectory](https://github.com/jaadt7/elliptical_trajectory)), MESA (B. Paxton et al. 2011, 2013, 2015, 2018, 2019; A. S. Jermyn et al. 2023, <https://docs.mesastar.org>).

## ORCID iDs

Jaad A. Tannous  <https://orcid.org/0000-0002-9970-6454>  
 G. Wendell Misch  <https://orcid.org/0000-0002-0637-0753>  
 Matthew R. Mumpower  <https://orcid.org/0000-0002-9950-9688>  
 Bradley S. Meyer  <https://orcid.org/0000-0001-6307-9818>  
 F. X. Timmes  <https://orcid.org/0000-0002-0474-159X>  
 Aaron Couture  <https://orcid.org/0000-0002-0861-3616>

Chris L. Fryer  <https://orcid.org/0000-0003-2624-0056>

## References

- Almaraz-Calderon, S., Rehm, K. E., Gerken, N., et al. 2017, *PhRvL*, **119**, 072701
- Birck, J. L., & Allegre, C. J. 1978, *E&PSL*, **39**, 37
- Brown, B. A., Chung, W., & Wildenthal, B. 1978, *PhRvL*, **40**, 1631
- Burbidge, E. M., Burbidge, G. R., Fowler, W. A., & Hoyle, F. 1957, *RvMP*, **29**, 547
- Clayton, D. D., & Rassbach, M. 1967, *ApJ*, **148**, 69
- Clayton, D. D., & Ward, R. A. 1974, *ApJ*, **193**, 397
- Coc, A., Porquet, M.-G., & Nowacki, F. 1999, *PhRvC*, **61**, 015801
- Cowan, J. J., Sneden, C., Lawler, J. E., et al. 2021, *RvMP*, **93**, 015002
- Cyburt, R. H., Amthor, A. M., Ferguson, R., et al. 2010, *ApJS*, **189**, 240
- Diehl, R., Halloin, H., Kretschmer, K., et al. 2006, *Natur*, **439**, 45
- El Eid, M. F., Meyer, B. S., et al. 2007, *ApJ*, **655**, 1058
- Frischknecht, U., Hirschi, R., Pignatari, M., et al. 2015, *MNRAS*, **456**, 1803
- Fuller, G. M., Fowler, W. A., & Newman, M. J. 1980, *ApJS*, **42**, 447
- Gallino, R., Arlandini, C., Busso, M., et al. 1998, *ApJ*, **497**, 388
- Gove, N., & Martin, M. 1971, *ADNDT*, **10**, 205
- Gupta, S. S., & Meyer, B. S. 2001, *PhRvC*, **64**, 025805
- Handley, T. H., & Lyon, W. S. 1955, *PhRv*, **99**, 755
- Hollowell, D., & Iben, I., Jr. 1990, *ApJ*, **349**, 208
- Holmbeck, E. M., Sprouse, T. M., & Mumpower, M. R. 2023, *EPJA*, **59**, 28
- Jermyn, A. S., Bauer, E. B., Schwab, J., et al. 2023, *ApJS*, **265**, 15
- Kajino, T., Aoki, W., Balantekin, A., et al. 2019, *PtNP*, **107**, 109
- Kippenhahn, R., Weigert, A., & Weiss, A. 1990, *Stellar Structure and Evolution*, Vol. 282 (Berlin: Springer).
- Langanke, K., & Martinez-Pinedo, G. 2000, *NuPhA*, **673**, 481
- Lee, T., Papanastassiou, D. A., & Wasserburg, G. J. 1977, *ApJL*, **211**, L107
- Lodders, K. 2003, *ApJ*, **591**, 1220
- Meyer, B. 2013, in *NIC XII (Treiste: SISSA)*, 96
- Meyer, B. S., & Adams, D. C. 2007, *M&PSA*, **42**, 5215
- Misch, G. W., Ghorui, S. K., Banerjee, P., Sun, Y., & Mumpower, M. R. 2020, *ApJS*, **252**, 2
- Misch, G. W., & Mumpower, M. R. 2024, *EPJST*, **233**, 1075
- Misch, G. W., Sprouse, T. M., Mumpower, M. R., et al. 2021, *Symm*, **13**, 1831
- Nabi, J., & Klapdor-Kleingrothaus, H. 2004, *ADNDT*, **88**, 237
- Paxton, B., Bildsten, L., Dotter, A., et al. 2011, *ApJS*, **192**, 3
- Paxton, B., Cantiello, M., Arras, P., et al. 2013, *ApJS*, **208**, 4
- Paxton, B., Marchant, P., Schwab, J., et al. 2015, *ApJS*, **220**, 15
- Paxton, B., Schwab, J., Bauer, E. B., et al. 2018, *ApJS*, **234**, 34
- Paxton, B., Smolec, R., Schwab, J., et al. 2019, *ApJS*, **243**, 10
- Prantzos, N., Abia, C., Cristallo, S., Limongi, M., & Chieffi, A. 2020, *MNRAS*, **491**, 1832
- Ratzel, U., Arlandini, C., Käppeler, F., et al. 2004, *PhRvC*, **70**, 065803
- Singh, B., & Chen, J. 2014, *NDS*, **116**, 1
- Stephan, T., Trappitsch, R., Davis, A. M., et al. 2018, *GeCoA*, **221**, 109
- Takahashi, K., & Yokoi, K. 1987, *ADNDT*, **36**, 375
- Tannous, J. 2025, Elliptical Trajectory Builder v1.0.0 Zenodo, doi: 10.5281/zenodo.14796677
- Tannous, J., & Meyer, B. S. 2023, *85Kr Isomer and the S Process* (Washington, DC: OSF).
- Turkat, S., Mougeot, X., Singh, B., & Zuber, K. 2023, *ADNDT*, **152**, 101584
- Ward, R. A., & Fowler, W. A. 1980, *ApJ*, **238**, 266
- Weisskopf, V., & Wigner, E. P. 1930, *ZPhy*, **63**, 54